The Astrophysical Journal, 578:868–876, 2002 October 20

THE RADIAL DISTRIBUTION OF COLD ATOMIC HYDROGEN IN THE GALAXY

Michal A. Kolpak, James M. Jackson, and T. M. Bania
Institute for Astrophysical Research, Boston University, 725 Commonwealth Avenue, Boston, MA 02215

and

John M. Dickey
Astronomy Department, University of Minnesota, 116 Church Street SE, Minneapolis, MN 55455
Received 2002 April 19; accepted 2002 June 27

ABSTRACT

H I absorption spectra measured against bright extragalactic radio continuum sources offer a simple way to measure the optical depth of cold atomic gas as a function of Galactocentric radius. We have observed the 21 cm H I line in absorption toward 54 bright, compact extragalactic radio continuum sources in the first Galactic quadrant with the VLA in C array. We have determined the average radial profile of 21 cm H I optical depth in the first quadrant using the Clemens rotation curve. There is a region of high average optical depth between Galactic radii of 4 and 8 kpc where the average optical depth, $\langle\tau(R)\rangle$, exceeds 0.8. This region also contains most of the molecular gas in the Galaxy. Furthermore, the highest peak in $\langle\tau(R)\rangle$ occurs in the region of the 5 kpc molecular ring, the Galaxy's single most prominent molecular feature. Inward of 4 kpc, $\langle\tau(R)\rangle$ drops below 0.5, and beyond 8.5 kpc, $\langle\tau(R)\rangle$ remains below 0.4. The H I optical depth measurements were used to construct the 21 cm H I velocity-averaged absorption coefficient, $\langle\kappa(R)\rangle$, as a function of Galactocentric radius. The average value of $\langle\kappa(R)\rangle$ exceeds 4.5 km s^{-1} kpc^{-1} between 4 and 8 kpc and drops sharply at smaller and larger radii. The highest peak in $\langle\kappa(R)\rangle$ rises above 15 km s^{-1} kpc^{-1} and again corresponds to the 5 kpc molecular ring. Two other large peaks correspond to the Sagittarius and Perseus spiral arms. We suggest that the high H I opacity in the inner Galaxy, particularly between 4 and 8 kpc, is due to the presence of cold atomic gas associated with molecular clouds.

Subject headings: Galaxy: general — Galaxy: structure — ISM: atoms — ISM: clouds — ISM: structure — radio lines: ISM — techniques: interferometric

1. INTRODUCTION

Observations of the 21 cm H I line toward bright radio continuum sources often reveal absorption features. Because the opacity of the 21 cm transition is proportional to gas column density divided by gas temperature, the coldest, densest gas produces the strongest H I absorption features. The large-scale spatial distribution of this cold dense atomic gas is still poorly known. Studying the morphology of cold H I will help answer important questions concerning the connection between this and other phases of the interstellar medium.

Garwood & Dickey (1989, hereafter GD89) derived the Galactic radial dependence of 21 cm H I opacity from absorption spectra toward 19 continuum sources. They measured the velocity-averaged absorption coefficient, $\langle\kappa(R)\rangle$, to be roughly 5 km s^{-1} kpc^{-1} between Galactic radii of 6 and 8.5 kpc. They also found that $\langle\kappa(R)\rangle$ drops by a factor of 2 between Galactocentric radii of 6 and 4 kpc. In the same region (between Galactocentric radii of 4 and 6 kpc), surveys of molecular emission from the inner Galaxy (e.g., Clemens, Sanders, & Scoville 1988, hereafter CSS88) have revealed the presence of a dense ring of molecular gas. This ring has also been interpreted as two spiral arms (the Scutum and 4 kpc arms) viewed tangentially (e.g., Cohen et al. 1980). This so-called 5 kpc molecular ring is the single most prominent molecular emission feature in the Galaxy. The decrease in 21 cm opacity inward of 6 kpc measured by GD89 therefore implies that the largest concentration of molecular material in the Galaxy is relatively deficient in cold atomic gas. This surprising result is inconsistent with a model of the interstellar medium (ISM) in which molecular clouds form within cold, dense concentrations of H I. This is an important result that should be independently tested by further measurements.

In the next section of this paper we describe our source selection criteria and observations, and in § 3 our methods of data reduction and analysis are presented. The results of our analysis are described in § 4. We present an interpretation and discussion of the results in § 5, and § 6 contains a summary of our main results.

2. OBSERVATIONS

We obtained 21 cm absorption spectra toward 149 radio continuum sources in the first quadrant of the Galactic plane ($l = 18°-46°$ and $b = \pm 0.°5$) using the VLA in C-array configuration at L band with 128 channels and a velocity resolution of 2.6 km s^{-1}. The FWHM of the synthesized beam was 16″. The total integration time for each source was typically 10–15 minutes, and spectra typically have rms fluctuations of 15 mJy beam^{-1}. Taking 289 arcsec^2 as a representative beam size, we calculate that 1 mJy beam^{-1} corresponds to a brightness temperature of 2.37 K.

2.1. *Sensitivity to* H I *Column Density*

The optical depth of H I absorption per velocity interval [in units of (km s^{-1})$^{-1}$] is given below by equation (1) (e.g., Kulkarni & Heiles 1988):

$$\tau_v = 5.5 \times 10^{-19} \frac{N_v}{T_{\rm spin}} \ . \qquad (1)$$

Here N_v is the column density of H I absorption per velocity interval and $T_{\rm spin}$ is the spin temperature (K) of the absorbing gas. The average continuum flux per beam of our observed sources is 85 mJy beam^{-1}. With spectral fluctuations of 15 mJy beam^{-1}, we therefore have a typical optical depth sensitivity of 0.2. Taking 50 K as a representative spin temperature for cold H I, this optical depth sensitivity corresponds to a column density of 1.8×10^{19} cm^{-2} (km s^{-1})$^{-1}$. The total column density of a cloud at our detection threshold is calculated by integrating over a typical H I absorption line, which has a FWHM of 5 km s^{-1}. We therefore expect to detect all cold H I clouds with total H I column densities greater than roughly 6.8×10^{19} cm^{-2}.

2.2. *Interferometer versus Single Dish*

Single dish observations of H I absorption require the subtraction of the background large-scale diffuse H I emission in the Galactic plane. Spatial variations in the level of H I emission over the source region make the subtraction difficult, and the uncertainty introduced by this subtraction is the dominant source of uncertainty in single dish H I absorption spectra (Dickey & Lockman 1990).

The problem of removing extended emission is ameliorated by using an interferometer to measure the H I absorption. Because interferometers have a minimum baseline length, they filter out spatial frequencies below a threshold value. The minimum baseline length for the C-array configuration of the VLA is 35 m. At *L* band, the threshold spatial scale is roughly 10′ for snapshot observations. Our observations are relatively insensitive to H I emission on angular scale sizes larger than this, and we therefore measure the H I absorption spectra directly, without position switching.

2.3. *Selection of Extragalactic Sources*

Our absorption spectra sample cold atomic hydrogen between the source and observer. The 21 cm radiation from extragalactic sources passes through the entire Galactic disk, whereas the radiation from Galactic sources preferentially samples the near side of the Galaxy. To avoid a bias toward conditions on the near side of the locus of tangent points, we used only extragalactic continuum sources in our analysis.

We identified extragalactic continuum sources by the presence of significant absorption at local standard of rest (LSR) velocities less than -10 km s^{-1}. This negative velocity absorption (NVA) is caused by material outside the solar circle. Because there are very few strong Galactic continuum sources in the outer Galaxy, the presence of NVA in the spectrum of a continuum source suggests that it is extragalactic. From our original sample of 149 radio continuum sources, we selected 54 sources whose spectra show NVA with optical depth greater than 0.4 in at least two consecutive channels.

To test whether our selection criterion does indeed discriminate between Galactic and extragalactic sources, we compared the positions of all 149 of our observed continuum sources with the hydrogen recombination line emission catalog compiled by Lockman (1989). This catalog contains nearly 500 thermal, Galactic recombination line sources in the northern sky. Only 30% of our 54 NVA-selected sources are within 3′ (one beamwidth for the recombination line survey) of any source in the recombination line catalog, while over 70% of the 95 sources without NVA are within 3′ of a source in Lockman's catalog.

We further studied the success of our source selection by estimating the expected number of chance coincidences between our 54 sources and the recombination line sources in Lockman's catalog. Our 54 sources are in 19 separately observed fields, and for each field, the FWHM of the primary beam is 32′. The effective area covered by our source sample is therefore 4.2 deg^2. A total of 63 sources from the Lockman catalog are within our effective source sample area. Coincidence is possible within a circle of 3′ radius around each of these 63 recombination line sources. The total area of possible coincidence is then 0.5 deg^2. The probability of a coincidence is the ratio of this area to the entire area covered by our source sample, or 12%. Therefore, nearly half of the coincidences between recombination line sources and our 54 NVA-selected extragalactic sources probably result from random chance.

Although the Lockman survey is incomplete below 1 Jy, the anticorrelation between the presence of NVA and recombination line emission provides support for our source selection technique. There may be a few Galactic sources included in our sample, but the majority are probably extragalactic. Thus, our measurements of H I absorption should not be biased toward conditions on the near side of the Galaxy.

2.4. *Effect of Latitude Range*

The cold, dense H I that is responsible for 21 cm absorption features has a vertical scale height of only 100 pc (e.g., Kulkarni & Heiles 1987). In order to sample cold H I on the far side of the tangent point and in the outer Galaxy, we therefore chose background continuum sources with relatively small Galactic latitudes. The absolute values of the Galactic latitudes of all of our 54 sight lines are less than 0°.7. Only nine of our sight lines rise above the cold H I scale height at Galactocentric radii smaller than 16 kpc, and only four rise above two scale heights inward of 16 kpc. Cold H I gas out to Galactocentric radii of at least 16 kpc should therefore be well sampled by our 54 lines of sight.

3. DATA REDUCTION AND ANALYSIS

3.1. *Data Reduction*

After the UV data were edited and calibrated, mosaicked dirty image cubes were created using MIRIAD (Sault, Teuben, & Wright 1995). We produced continuum maps by averaging together line-free channels (typically a total of 50 channels). These continuum maps were used to identify the positions of bright continuum sources as well as to measure their total fluxes. A primary-beam correction was automatically applied to the continuum images using the MIRIAD task *invert*. This automatic correction was tapered in order to keep the noise level roughly constant across each field. As a consequence, the map regions farthest from the field center are significantly undercorrected. Our measurements of the total flux from each source are therefore lower limits. This effect is largest for the sources that are most distant from the field centers.

Spectra for each of the 54 extragalactic continuum sources were obtained by spatially averaging together the brightest central pixels of the dirty cube, typically over an area of 200–300 arcsec^2. We measured the continuum flux level for

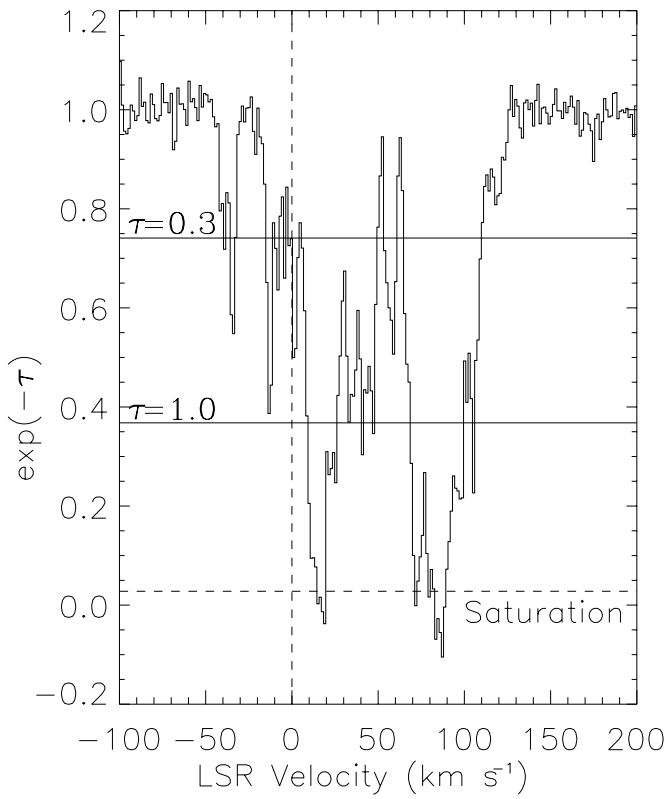

FIG. 1.—21 cm H I absorption spectrum for source G31.389−0.383 is plotted as a function of LSR velocity. The measured spectrum was divided by the continuum level and represents $\exp(-\tau)$. This source has a flux density of 0.50 Jy beam^{-1}. The spectral baseline rms is 0.014 Jy beam^{-1}. Optical depths of 0.3 and 1 are indicated by horizontal solid lines, and the saturation level (defined to be 1 σ above zero) is marked by the horizontal dotted line. Note that there is significant absorption from gas beyond the solar circle (negative velocities).

each source by fitting a first-order baseline to the average spectrum. A representative spectrum is shown in Figure 1, and important parameters of the 54 extragalactic continuum sources are listed in Table 1. Column (1) lists source names of the 54 extragalactic radio continuum sources used in our analysis. The J2000.0 right ascension and declination for each source are listed in columns (2) and (3). Column (4) contains the total flux for each source, and column (5) lists the average flux per beam for each continuum source. The rms fluctuation of the baseline of the absorption spectrum for each source is listed in column (6), and column (7) contains the corresponding fluctuation in the optical depth spectrum.

3.2. *Measuring* $\langle\tau(R)\rangle$

The first step in our analysis was to measure the rms fluctuation in the baseline of each spectrum (hereafter σ). We then measured the optical depth of each useful channel (a total of over 7000 measurements). Because of baseline fluctuations near the edges of the bandpass, we used only channels that were at least 15 km s^{-1} from the edges ($\sim$−80 to $\sim$180 km s^{-1}). Roughly 15% of all measured channels had intensities within 1 σ of zero and were therefore considered to be saturated. Our measurements of optical depth for these saturated channels are lower bounds. To calculate these lower bounds, we assume that the minimum intensity we can reliably measure is 1 σ. The lower bound for the optical depth of saturated points, $\tau_{\rm lb}$, is then given by

$$\tau_{\rm lb} = -\ln\left(\frac{\sigma}{F_c}\right) . \quad (2)$$

In this expression, F_c represents the average flux per beam from the continuum source. For each continuum source, this average was taken over the same area that was used to produce the absorption spectrum.

We used the Clemens (1985, hereafter C85) rotation curve to find the Galactocentric radius corresponding to the longitude and velocity of each optical depth measurement. The total number of measured optical depths as a function of Galactocentric radius is shown in Figure 2. We constructed 0.5 kpc radial bins and computed the weighted average of the optical depth in each bin. Each measurement was weighted by $(F_c/\sigma)^2$ in order to emphasize data of higher quality. Because the depth of an absorption feature is directly proportional to the brightness of the background source, F_c, the quantity $(F_c/\sigma)^2$ is proportional to the square of the signal-to-noise ratio of each optical depth measurement. We excluded channels with velocities greater than 10 km s^{-1} above the tangent point velocity for each line of sight, unless the optical depth at those velocities exceeded 0.1. This was done to exclude meaningless noise from the averages while including absorption caused by clouds near the tangent point with large streaming motions.

None of the lines of sight to our sources passes nearer than 2.5 kpc to the Galactic center, and so we have no

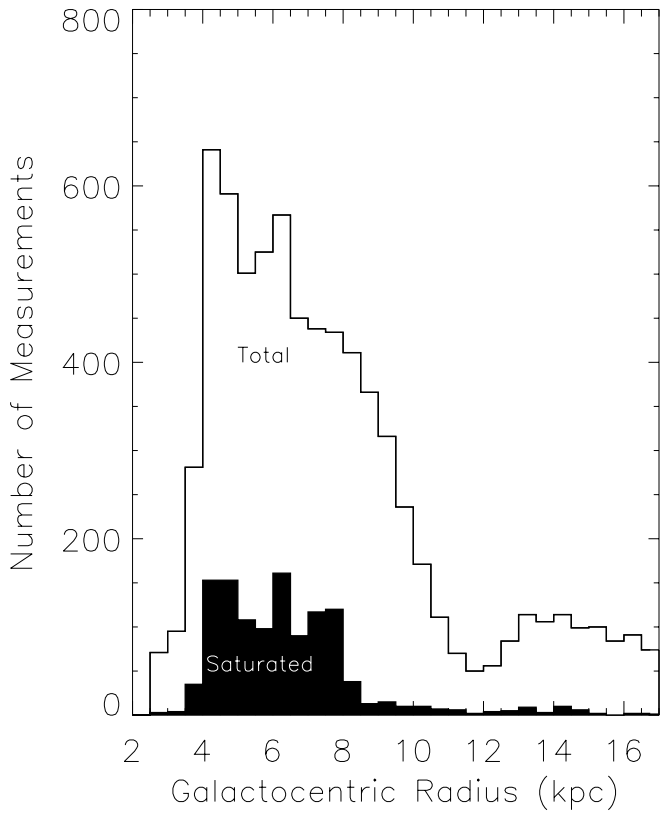

FIG. 2.—Total number of optical depth measurements is plotted as a function of Galactocentric radius. The smaller, shaded curve indicates the number of saturated measurements (lower bounds). The Galactocentric radius of each measurement was determined using the Clemens (1985) rotation curve.

TABLE 1

RADIO CONTINUUM SOURCES

Source	R.A. (J2000.0)	Decl. (J2000.0)	F_t (mJy)	F_c (mJy beam^{-1})	σ (mJy beam^{-1})	σ_τ
G18.181−0.390.....	18 25 28.2	−13 16 46.9	2610	22	2	0.10
G18.674−0.237.....	18 25 51.6	−12 46 20.3	480[a]	92	12	0.14
G19.491+0.135.....	18 26 04.4	−11 52 34.0	190[a]	115	18	0.17
G23.817+0.224.....	18 33 53.9	−08 00 06.4	130	11	3	0.32
G24.131+0.122.....	18 34 50.9	−07 46 12.3	170	30	7	0.27
G24.180+0.564.....	18 33 21.3	−07 31 22.4	370	225	20	0.09
G24.463+0.245.....	18 35 01.4	−07 25 07.5	710	149	15	0.11
G24.541+0.599.....	18 33 54.1	−07 11 11.2	240	142	14	0.10
G25.237−0.150.....	18 37 52.4	−06 54 46.6	360	207	13	0.06
G25.252−0.139.....	18 37 51.7	−06 53 40.5	360	101	15	0.16
G25.267−0.161.....	18 37 58.0	−06 53 28.9	490	243	12	0.05
G25.395+0.033.....	18 37 30.6	−06 41 18.9	310	158	16	0.11
G25.457−0.211.....	18 38 29.9	−06 44 43.7	180	72	8	0.12
G25.605−0.037.....	18 38 08.9	−06 32 02.9	300	172	16	0.10
G26.532+0.426.....	18 38 12.3	−05 29 53.0	100	42	5	0.13
G28.556+0.018.....	18 43 22.8	−03 53 07.8	560	45	9	0.22
G28.580−0.076.....	18 43 45.6	−03 54 25.6	370[a]	56	9	0.18
G28.600−0.119.....	18 43 57.0	−03 54 32.3	740[a]	42	5	0.13
G28.609+0.018.....	18 43 28.6	−03 50 18.1	380	83	9	0.11
G28.669−0.111.....	18 44 02.8	−03 50 38.2	1080	51	9	0.19
G28.700+0.046.....	18 43 32.6	−03 44 40.6	720	40	4	0.11
G28.759+0.280.....	18 42 49.1	−03 35 06.7	340	23	5	0.25
G28.789+0.242.....	18 43 00.5	−03 34 33.2	320	31	5	0.18
G28.998+0.073.....	18 43 59.6	−03 28 02.0	400	16	2	0.13
G29.090+0.511.....	18 42 36.1	−03 11 06.7	150[a]	74	11	0.16
G30.234−0.139.....	18 47 00.6	−02 27 51.7	400	171	13	0.08
G30.996−0.299.....	18 48 58.2	−01 51 33.3	140	92	12	0.14
G31.013+0.334.....	18 46 44.9	−01 33 19.3	100[a]	64	16	0.29
G31.051+0.089.....	18 47 41.4	−01 37 60.0	140[a]	29	11	0.48
G31.070+0.049.....	18 47 52.0	−01 38 4.8	390	74	12	0.18
G31.280+0.063.....	18 48 12.0	−01 26 29.1	290	104	15	0.16
G31.389−0.383.....	18 49 59.2	−01 32 52.1	980	501	14	0.03
G31.866+0.063.....	18 49 16.2	00 55 11.7	3000[a]	89	6	0.07
G33.812−0.190.....	18 53 43.2	00 41 47.8	220	120	15	0.13
G34.133+0.470.....	18 51 57.3	01 16 59.7	240[a]	82	14	0.19
G34.386+0.655.....	18 51 45.5	01 35 33.9	280[a]	104	11	0.11
G35.308+0.145.....	18 55 15.4	02 10 50.6	100	26	11	0.55
G35.351+0.238.....	18 55 0.3	02 15 41.1	90	42	13	0.37
G35.467+0.139.....	18 55 34.1	02 19 10.1	210	83	6	0.08
G35.484+0.424.....	18 54 35.1	02 27 52.6	40[a]	25	11	0.58
G37.462−0.230.....	19 00 32.1	03 55 32.4	1850	36	2	0.06
G37.645−0.098.....	19 00 24.0	04 08 55.6	610	49	3	0.06
G37.867−0.601.....	19 02 36.0	04 06 57.6	180	87	12	0.15
G42.026−0.604.....	19 10 18.0	07 48 28.7	60[a]	16	2	0.13
G42.091−0.430.....	19 09 47.9	07 56 45.4	30[a]	14	2	0.15
G42.110−0.445.....	19 09 53.3	07 57 21.2	110[a]	9	1	0.12
G42.114−0.622.....	19 10 31.7	07 52 39.7	350[a]	7	1	0.15
G42.177−0.519.....	19 12 08.8	08 52 04.2	160	73	4	0.06
G43.294−0.645.....	19 12 49.1	08 54 47.4	40	22	5	0.26
G45.069+0.141.....	19 13 19.9	10 51 00.9	270	83	7	0.09
G45.828−0.290.....	19 16 19.5	11 19 18.7	210	33	4	0.13
G45.876−0.613.....	19 17 34.9	11 12 49.0	30	9	6	1.10
G46.036−0.001.....	19 15 40.6	11 38 25.9	30[a]	31	8	0.30
G46.091−0.246.....	19 16 40.0	11 34 30.1	40	17	6	0.44

NOTE.—Units of right ascension are hours, minutes, and seconds, and units of declination are degrees, arcminutes, and arcseconds.

[a] These sources are more than 20′ from their respective field centers, and their total flux measurements are significantly underestimated.

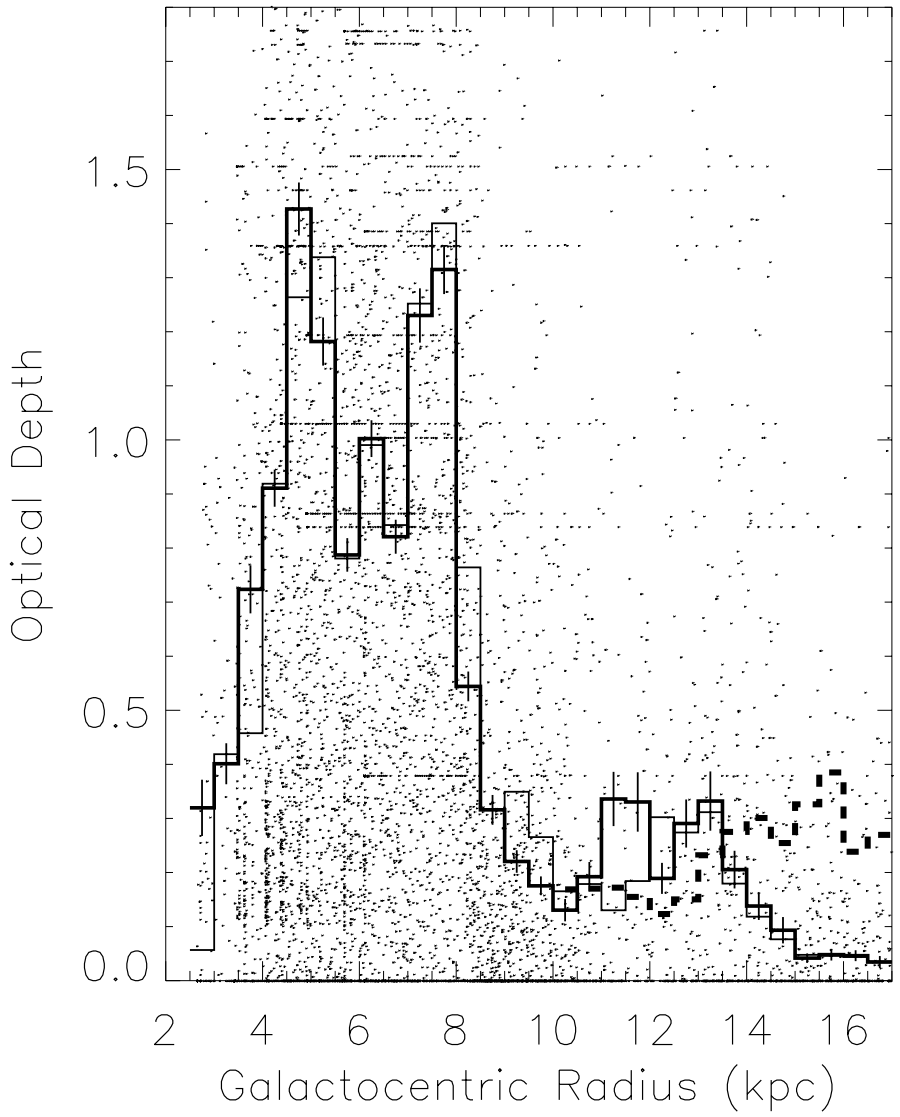

FIG. 3.—Measured optical depth of 21 cm H I absorption is plotted against Galactocentric radius. Individual channel measurements are represented by dots. Optical depths as high as 3.5 were measured, but the plot range has been restricted to emphasize the radial variation in the mean values. The dark solid histogram shows the weighted mean value in each 0.5 kpc bin computed using the C85 rotation curve, the light solid histogram is the analogous result for a flat rotation curve, and the dashed histogram is the result for the flat-linear rotation curve. The full length of each error bar represents twice the weighted standard deviation of the measurements in that radial bin. To avoid confusion, we plot error bars only for the result computed using the C85 rotation curve, but error bars for the results computed using the other rotation curves are very similar. The horizontal lines of points are artifacts caused by line saturation. Between radii of 4 and 8 kpc, the average optical depth exceeds 0.8, and the histograms for the three rotation curves are almost identical. The location and size of the peaks beyond 10 kpc are strongly dependent on the choice of rotation curve.

measurements at smaller radii. In the outer Galaxy, we limited our analysis to Galactocentric radii less than 17 kpc because we measure no significant H I absorption at velocities corresponding to distances beyond 17 kpc.

Kinematically derived Galactocentric radii vary slightly depending on the details of the rotation curve used to calculate them. In order to test whether the variations in the assumed shape of the Galactic rotation curve would affect our results, we computed the radial profile of $\langle\tau(R)\rangle$ again, using a flat rotation curve ($R_0 = 8.5$ kpc, $V = 220$ km s^{-1} for all radii). We then computed $\langle\tau(R)\rangle$ a third time using a rotation curve that is flat ($R_0 = 8.5$ kpc, $V = 220$ km s^{-1}) for Galactocentric radii less than 10 kpc and increases linearly from $V = 220$ km s^{-1} at $R_0 = 10.0$ kpc to $V = 300$ km s^{-1} at $R_0 = 20.0$ kpc. We will hereafter refer to this third rotation curve as the flat-linear rotation curve. The results for all three rotation curves are presented together in Figure 3 and are discussed below.

3.3. *Measuring* $\langle\kappa(R)\rangle$

Although a measurement of $\langle\tau(R)\rangle$ indicates the large-scale structure of cold atomic gas in the Galaxy, the velocity-averaged absorption coefficient, κ, is a more fundamental physical parameter. First of all, because of Galactic rotation, the radial velocity gradient within the Galaxy depends on both Galactic longitude and radial velocity. Optical depths measured in channels of fixed width therefore correspond to different path lengths and are not strictly comparable. The absorption coefficient, κ, on the other hand, is weighted by path length and therefore does not suffer the same problem. Another advantage of using κ is that

it refers to gas at a specific location in the Galaxy, independent of viewing geometry. In contrast, any measurement of optical depth is referenced to a specific line of sight and is not a general characteristic of the gas.

In the high-latitude local ISM, κ has been measured to have a value between 5 and 7 km s^{-1} kpc^{-1} (Dickey et al. 1981). To test the variation of this parameter within the Galaxy, we first computed $\kappa(R)$ as a function of Galactocentric radius (in 0.5 kpc radial bins) along the line of sight to each continuum source:

$$\kappa(R)\Delta S(R) = \int \tau \, dv \, . \tag{3}$$

Here the integral is taken over a velocity range corresponding to the radial bin. The C85 rotation curve was used to compute these limits. The quantity ΔS is the line-of-sight path length through the radial bin. We then computed the weighted mean value of κ in each bin for all of the continuum sources. The values of κ for the individual sources were weighted by the line-of-sight distance through each radial bin as well as by $(F_c/\sigma)^2$. Weighting by the path length serves to emphasize sight lines that sample a larger and hence more representative sample of a given radial bin. Because we included saturated channels, our measurements of $\langle\kappa(R)\rangle$ are also lower bounds.

4. RESULTS

4.1. H I *Optical Depth*

Our derivation of the average 21 cm H I optical depth as a function of Galactocentric radius is shown in Figure 3 (*dark solid histogram*). Between radii of 4 and 8 kpc, $\langle\tau(R)\rangle$ is greater than 0.8, and there are two peaks where $\langle\tau(R)\rangle$ exceeds 1.3. In this region of large $\langle\tau(R)\rangle$, we measured optical depths as high as 3.5. Each radial bin in this region contains at least 400 channel measurements.

There is a significant decrease in the average H I optical depth inward of 4 kpc. Although our source sample has a large longitude gap between 19°.5 and 23°.8, eight of our sight lines sample gas at Galactocentric radii inward of 4 kpc. Our lower bound on $\langle\tau(R)\rangle$ for the bin centered at 3.75 kpc is 0.7, and between 2.5 and 3.5 kpc it does not exceed 0.4. The three bins inward of 4 kpc each contain at least 50 measurements.

At radii larger than 8 kpc, $\langle\tau(R)\rangle$ also drops sharply and remains below 0.35 beyond 8.5 kpc. Two peaks in $\langle\tau(R)\rangle$, centered at 11.5 and 13 kpc rise above 0.3. Beyond 14.5 kpc, $\langle\tau(R)\rangle$ remains below 0.1. The radial bins outward of 8 kpc each contain more than 50 measurements.

In Figure 3 we compare the histogram for the flat rotation curve (*light, solid histogram*) and the flat-linear rotation curve (*dashed histogram*) to the result using the C85 rotation curve. In contrast to the flat and flat-linear rotation curves, the C85 rotation curve oscillates several times between 2 and 13 kpc, with the rotation speed ranging in value from 195 to 225 km s^{-1} and a mean value of roughly 215 km s^{-1}. Nonetheless, the choice of rotation curve clearly has little effect on the general character of our results in the inner Galaxy. The high-$\langle\tau(R)\rangle$ region between 4 and 8 kpc, as well as the two large peaks within this region, are present regardless of which rotation curve is adopted.

In contrast, the presence of the minor peaks in the outer Galaxy depends on which rotation curve is used to derive $\langle\tau(R)\rangle$. Consequently, the reality of these peaks is uncertain. The optical depth peak between 11 and 12 kpc is present in the result obtained using the C85 rotation curve but is absent in the profiles derived with the flat and flat-linear rotation curves. The 13 kpc peak is present in the results obtained with the C85 and the flat rotation curves (the C85 rotation curve is flat beyond 13 kpc). On the other hand, when the flat-linear rotation curve is used to compute the histogram, the 13 kpc peak is absent. In its place, there is a broad peak between 13 and 17 kpc where the average optical depth exceeds 0.2. We therefore conclude that the reality of any optical depth peaks beyond 10 kpc is highly uncertain owing to the strong dependence of the optical depth profile on the choice of rotation curve. Further support for this conclusion is provided by Lockman (1988), who showed that the derived surface density of H I in the outer Galaxy is very sensitive to the slope of the rotation curve used.

4.2. H I *Absorption Coefficient*

In Figure 4 our measurement of the average 21 cm H I velocity-averaged absorption coefficient, $\langle\kappa(R)\rangle$, is plotted as a function of Galactic radius (*bold histogram*). In general, the shape of the profile is analogous to that of $\langle\tau(R)\rangle$. Throughout the high-$\langle\tau(R)\rangle$ region between 4 and 8 kpc, $\langle\kappa(R)\rangle$ is greater than 4.5 km s^{-1} kpc^{-1}. There are two large peaks where $\langle\kappa(R)\rangle$ rises above 13 km s^{-1} kpc^{-1}.

Inward of 4 kpc, $\langle\kappa(R)\rangle$ drops sharply and continues to decrease inward to 2.5 kpc, where it has a value of 3.6 km s^{-1} kpc^{-1}. Beyond 8 kpc, $\langle\kappa(R)\rangle$ also drops sharply, but there are significant peaks centered at 8.75, 11.25, and 13.25 kpc. Beyond 14 kpc, $\langle\kappa(R)\rangle$ is less than 0.5 km s^{-1} kpc^{-1}.

We did not compute $\langle\kappa(R)\rangle$ for either the flat rotation curve or the flat-linear rotation curve, because, based on the results for $\langle\tau(R)\rangle$, the results for $\langle\kappa(R)\rangle$ will be similar for any of the three rotation curves. We emphasize that the existence of the peaks in $\langle\kappa(R)\rangle$ at 11.25 and 13.25 kpc is probably very sensitive to the choice of rotation curve.

5. DISCUSSION

5.1. *Comparison to Previous Measurements*

Our measurement of $\langle\kappa(R)\rangle$ clearly disagrees with that of GD89, and this disagreement can be seen directly in Figure 4 (*bottom*). Instead of a steady drop between radii of 6 and 4 kpc, we find that $\langle\kappa(R)\rangle$ rises dramatically to a local maximum at 4.75 kpc. Also, instead of a roughly constant value of $\langle\kappa(R)\rangle$ between 6 and 8 kpc, we find that $\langle\kappa(R)\rangle$ is highly variable at these radii, ranging from 4.0 to 13.8 km s^{-1} kpc^{-1}.

5.1.1. *Differences in Velocity Selection*

It should be noted that in their analysis, GD89 excluded velocities within 5 km s^{-1} of the tangent point velocity. This was done to avoid regions with a small velocity gradient. In many of the spectra toward our 54 extragalactic continuum sources, however, the strongest absorption features occur at velocities near the tangent point. For our 54 sources, the tangent point radii range from 2.65 to 6.12 kpc. We would therefore expect that the exclusion of gas near the tangent point velocities would result in a significant underestimate of $\langle\kappa(R)\rangle$ for all radial bins inward of 6.5 kpc. For this reason, we did not exclude these velocities in the above analysis.

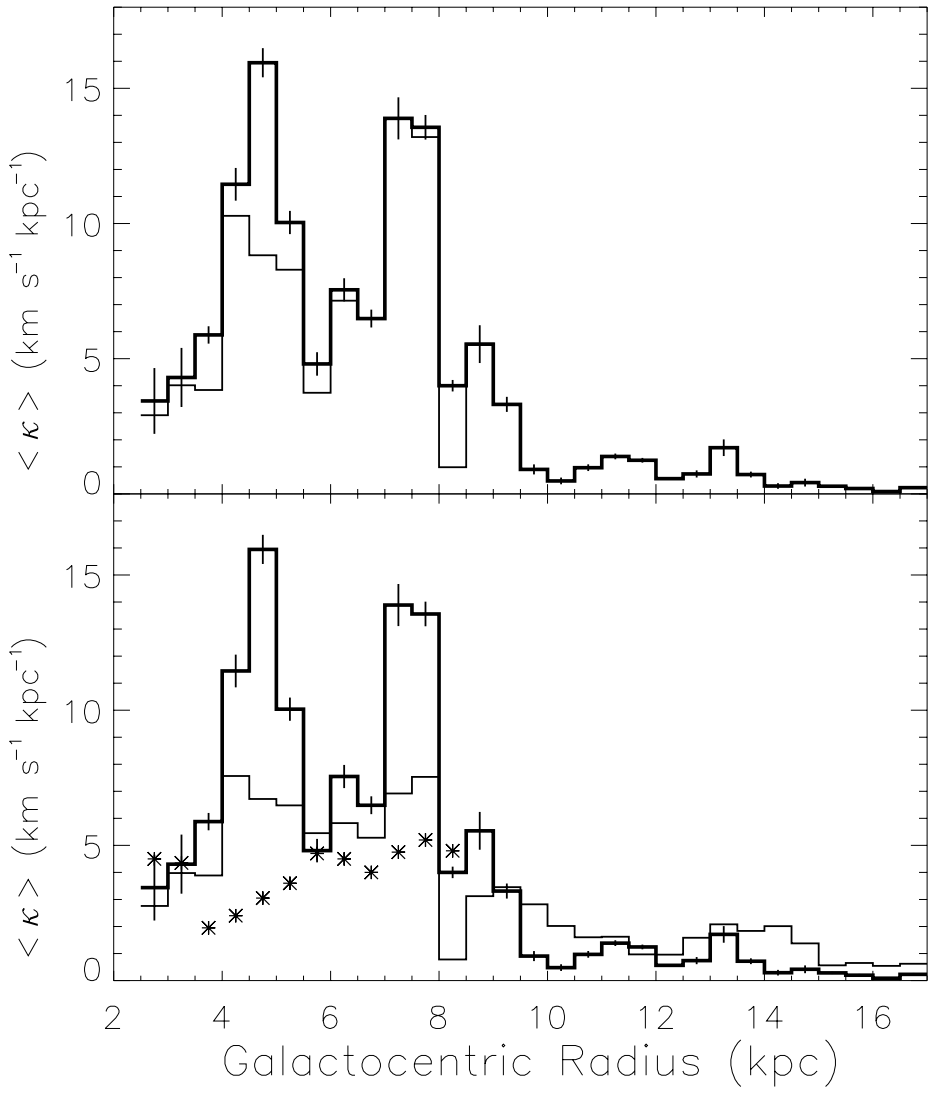

FIG. 4.—21 cm H I velocity-averaged absorption coefficient is plotted against Galactocentric radius. *Top:* The dark histogram represents the weighted average of all 54 extragalactic continuum sources. The light histogram shows the result of excluding gas within 5 km s^{-1} of the tangent point velocity for each source and gas with $|v| < 5$ km s^{-1}. The full length of each error bar represents twice the weighted standard deviation of the individual measurements in that radial bin. To avoid confusion, we plot error bars only for the result computed using our original weighting scheme and velocity selection criteria, but error bars for the results computed using the weighting scheme and/or the velocity selection criteria of GD89 are very similar. The three peaks between 4 and 9 kpc correspond to the three largest molecular gas concentrations in the first quadrant. *Bottom:* The dark histogram represents the weighted average of all 54 extragalactic continuum sources. The light histogram shows the result adopting the weighting scheme and velocity selection criteria of GD89. The stars mark the path-weighted average values of κ measured by GD89 (taken from GD89, top of Fig. 3).

Velocities with absolute values smaller than 5 km s^{-1} were also excluded by GD89 in order to avoid regions where the radial velocity of the gas is dominated by noncircular motions. Unlike the results of GD89, our measurement of $\langle\kappa(R)\rangle$ extends beyond the solar circle, and we included low-velocity ($|v| < 5$ km s^{-1}) gas in order to avoid artificially depressing the value of $\langle\kappa(R)\rangle$ near the solar circle. It is possible that this gas also contributes significantly to the large peak at 7.5 kpc in our derivation of $\langle\kappa(R)\rangle$.

In order to better understand the differences between our results and those of GD89, we calculated $\langle\kappa(R)\rangle$ a second time, excluding, as they did, all velocities within 5 km s^{-1} of the tangent point velocity and all velocities with absolute values smaller than 5 km s^{-1}. The resulting profile is shown as the light histogram in Figure 4 (*top*).

When we analyze our data with the GD89 velocity selection criteria, we do not reproduce their result. Specifically, we do not recover the factor of 2 decrease from 6 to 4 kpc found by GD89. Excluding the low-velocity gas near the solar circle reduces $\langle\kappa(R)\rangle$ in radial bins between 7.5 and 9 kpc, and the drop in opacity at 8 kpc becomes more pronounced. The peak between 7 and 8 kpc remains strong, however, and $\langle\kappa(R)\rangle$ is clearly not constant between 6 and 8 kpc, as found by GD89. The exclusion of tangent point gas reduces the value of $\langle\kappa(R)\rangle$ for all radial bins inward of 6.5 kpc as expected, and the effect is strongest between 4.5 and 5 kpc. Although the height of the peak at 5 kpc is reduced, there is still a pronounced increase in $\langle\kappa(R)\rangle$ between 6 and 4 kpc.

5.1.2. *Differences in Weighted Averages*

Another difference between our analysis and that of GD89 is the weighting used in averaging the $\kappa(R)$ for all the lines of sight. While we weighted each value by $[\Delta S(R)][(F_c/\sigma)^2]$, GD89 simply weighted by $[\Delta S(R)]$. To test if the different weightings can account for the differences between our results and those of GD89, we repeated the calculation of $\langle\kappa(R)\rangle$ a third time using their weighting scheme as well as their velocity selection criteria. The profile resulting from this third analysis is shown as the light histogram in Figure 4 (*bottom*).

The differences between our results and those of GD89 are not due to the different weighting schemes used. Although the change in weighting dramatically effects the size of the two peaks at 5 and 7.5 kpc, the profile still has the same general shape. There is a high-opacity region between 4 and 8 kpc, and $\langle\kappa(R)\rangle$ rises inward of 6 kpc.

5.1.3. *Differences in Source Sample*

Another important factor that could be responsible for the difference between our results and those of GD89 is the difference in the source samples used. Compared to our 54 sources, only 19 sources were used by GD89 to measure $\langle\kappa(R)\rangle$. Furthermore, spectra for 50 of our sources sample gas inward of 6 kpc, compared to only 12 sources from the sample of GD89. Because our sample size is larger, particularly inward of 6 kpc, our average opacity measurements will be less heavily effected by the presence of isolated clouds or voids along a few lines of sight and hence more representative of true azimuthally averaged radial maxima than the measurements of GD89. It seems plausible that the surprising results found by GD89 are strongly effected by small number statistics.

5.2. *Correlation with Molecular Gas*

Because molecular clouds form in cold dense environments, one would expect that the presence of cold, dense H I is correlated with the presence of molecular gas. This expectation has both theoretical and observational support. Photodissociation models predict that most molecular clouds should have cold H I envelopes (e.g., Wolfire, Hollenbach, & Tielens 1993), and several previous observational studies have found a correlation between the presence of molecular gas and H I self-absorption (e.g., Knapp 1974; Burton, Liszt, & Baker 1978; Bania & Lockman 1984; Jackson et al. 2002). Although GD89 measured relatively small values of $\langle\kappa(R)\rangle$ in the region of the 5 kpc molecular ring (2–4 km s^{-1} kpc^{-1}), they reported a strong spatial correlation between 21 cm H I absorption features and molecular emission lines in general.

The shape of our measured $\langle\kappa(R)\rangle$ radial profile provides further strong evidence that cold H I in the Galaxy is physically associated with molecular gas. There is a striking correlation between our measurement of $\langle\kappa(R)\rangle$ and the radial distribution of molecular mass (e.g., Fig. 11 in CSS88).

We measure peaks in the H I opacity at the locations of several prominent molecular features. For example, the largest peak in H I opacity occurs between 4 and 5.5 kpc, where $\langle\kappa(R)\rangle$ exceeds 15 km s^{-1} kpc^{-1}. This is also the location of the 5 kpc molecular ring. The second largest peak in $\langle\kappa(R)\rangle$ occurs between 7 and 8 kpc, which is roughly the location of the Sagittarius spiral arm. Finally, there is a small peak between 8.5 and 9 kpc, which is the location of the Perseus spiral arm. In the first Galactic quadrant, the 5 kpc molecular ring and the Sagittarius and Perseus spiral arms contain 73% of the molecular mass between radii of 1.5 and 16 kpc (CSS88).

The correspondence between high values of $\langle\kappa(R)\rangle$ and major concentrations of molecular mass is shown directly in Figure 5. Our measured profile of $\langle\kappa(R)\rangle$ is represented by the dark histogram, and the radial profile of molecular mass measured by CSS88 (taken from their Fig. 11) is shown by the light histogram. The molecular mass profile represents the total mass of molecular gas contained in 0.5 kpc wide circular annuli. Because these two profiles have different units, we have scaled the molecular mass profile so that the maximum value matches the maximum value of $\langle\kappa(R)\rangle$. We include the molecular mass profile strictly as an indication of the relative mass as a function of Galactocentric radius. While the three major peaks in molecular mass are not exactly coincident with the three peaks in $\langle\kappa(R)\rangle$, it is clear from this figure that most of the molecular gas in the Galaxy is contained in the regions of highest H I opacity.

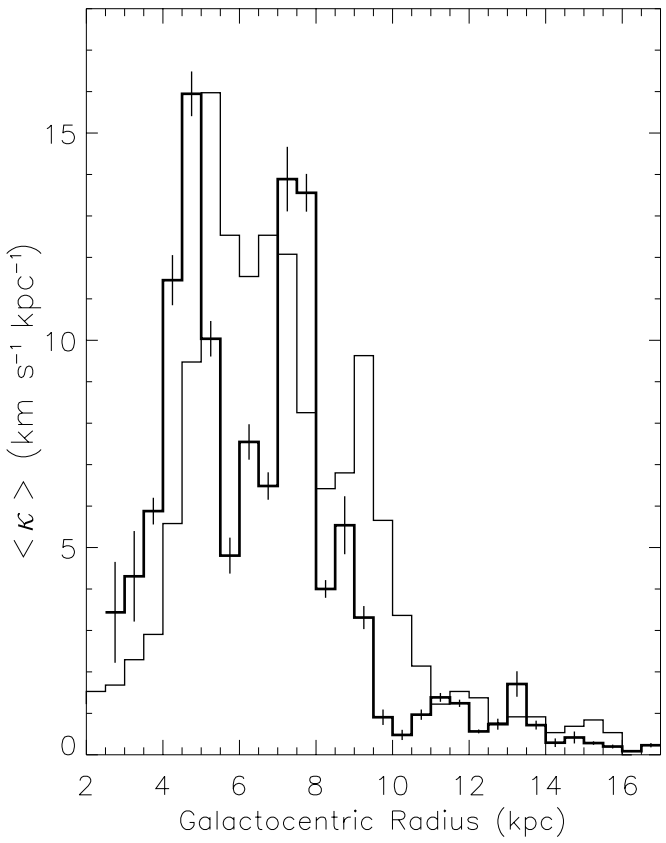

FIG. 5.—21 cm H I velocity-averaged absorption coefficient is plotted against Galactocentric radius. The dark histogram represents the weighted average of all 54 extragalactic continuum sources. Error bars are the same as in Fig. 4. The light histogram shows the radial profile of molecular gas mass derived by CSS88. This mass profile has been scaled vertically so that its peak is at the same level as our measured peak in $\langle\kappa(R)\rangle$. At its peak, the mass profile reaches a value of 3.7×10^8 $M_\odot$. Our measured peaks in $\langle\kappa(R)\rangle$ coincide with the largest molecular mass concentrations in the Galaxy.

6. SUMMARY

We have used 21 cm H I absorption spectra toward 54 extragalactic continuum sources to measure the galactocentric radial profiles of $\langle\tau(R)\rangle$ and $\langle\kappa(R)\rangle$ in the Galaxy. There is a region of high H I opacity between 4 and 8 kpc, where $\langle\tau(R)\rangle$ is greater than 0.8 and $\langle\kappa(R)\rangle$ is greater than 4.5 km s^{-1} kpc^{-1}. These results strongly disagree with those of GD89, who found a relatively constant H I opacity between 8 and 6 kpc and a 50% drop inward of 6 kpc. The GD89 result most likely suffers from the small number of sight lines they used to probe the radial profile of 21 cm absorption interior to 6 kpc. Between 2.5 and 3.5 kpc, we find that $\langle\tau(R)\rangle$ is less than 0.4 and $\langle\kappa(R)\rangle$ is less than 4.5 km s^{-1} kpc^{-1}. A peak at 9 kpc, where $\langle\kappa(R)\rangle$ is greater than 5 km s^{-1} kpc^{-1}, corresponds to the Perseus spiral arm. The existence of opacity peaks beyond 10 kpc is highly uncertain because the radial opacity profile in the outer Galaxy is highly sensitive to the choice of rotation curve. In general, we find that H I opacity is strongly correlated with the presence of molecular gas. The two largest opacity peaks correspond to the 5 kpc molecular ring and the Sagittarius spiral arm. The strong agreement between the radial profile of molecular gas and the measured profile of H I opacity suggests that cold H I is physically associated with molecular gas.

This work was supported in part by NSF grants AST 98-00334 and AST 00-98562. The authors would like to thank Harvey Liszt for very useful suggestions and comments.

REFERENCES

Bania, T. M., & Lockman, F. J. 1984, ApJS, 54, 513
Burton, W. B., Liszt, H. S., & Baker, P. L. 1978, ApJ, 219, L67
Clemens, D. P. 1985, ApJ, 295, 422
Clemens, D. P., Sanders, D. B., & Scoville, N. Z. 1988, ApJ, 327, 129
Cohen, R. S., Cong, H., Dame, T. M., & Thaddeus, P. 1980, ApJ, 239, L53
Dickey, J. M., & Lockman, F. J. 1990, ARA&A, 28, 215
Dickey, J. M., Weisberg, J. M., Rankin, J. M., & Boriakoff, V. 1981, A&A, 101, 332
Garwood, R. W., & Dickey, J. M. 1989, ApJ, 338, 841
Jackson, J. M., Bania, T. M., Simon, R., Kolpak, M. A., Clemens, D. P., & Heyer, M. 2002, ApJ, 566, L81
Knapp, G. R. 1974, AJ, 79, 527
Kulkarni, S. R., & Heiles, C. 1987, in Interstellar Processes, ed. D. J. Hollenbach & H. A. Thronson, Jr. (Dordrecht: Reidel), 87
———. 1988, in Galactic and Extragalactic Radio Astronomy, ed. G. L. Verschuur, & K. I. Kellermann (2d ed.; Berlin: Springer), 95
Lockman, F. J. 1988, in The Outer Galaxy, ed. L. Blitz & F. J. Lockman (Berlin: Springer), 79
———. 1989, ApJS, 71, 469
Sault, R. J., Teuben, P. J., & Wright, M. C. H. 1995, in ASP Conf. Ser., 77, Astronomical Data Analysis Software and Systems IV, ed. R. Shaw, H. E. Payne, & J. J. E. Hayes (San Francisc0: ASP), 433
Wolfire, M. G., Hollenbach, D., & Tielens, A. G. G. M. 1993, ApJ, 402, 195